



Atomically Dispersed Fe–N–S-Doped Carbon as an Efficient Li–S Battery Host for Capturing Polysulfides

Jihyeon Kang¹ · Jongkwon Park¹ · Myeong-Lok Seol² · Inho Nam¹ · Won Suk Jung³

Received: 8 September 2023 / Revised: 16 November 2023 / Accepted: 23 November 2023 / Published online: 15 February 2024
© The Author(s), under exclusive licence to Korean Institute of Chemical Engineers, Seoul, Korea 2024

Abstract

Lithium–sulfur batteries (LSBs) have emerged as promising candidates for advanced energy storage systems, due to their remarkable theoretical capacity of 1675 mAh g⁻¹ and specific energy density of 2600 Wh kg⁻¹, surpassing those of conventional Li-ion batteries. The abundance and cost-efficiency of sulfur make LSBs attractive in further. However, practical applications of LSBs face challenges such as the insulating nature of sulfur, migration of soluble lithium polysulfide (LIPS), and sluggish redox kinetics. Carbon-based materials have been explored to circumvent these barriers; however, their weak physical interactions limit their effectiveness. Heteroatom doping has shown the potential for anchoring LIPS; but optimization remains a challenge. In this study, we introduce a novel approach involving the synthesis of uniformly dispersed iron on activated carbon (AC, Ketjen black) as a support, yielding a single iron–nitrogen–sulfur-doped carbon (Fe–NSC) composite. This composite exhibited the following advantages as an LSB host: superior dispersion of the Fe catalyst, induced high surface area, and an increased proportion of Fe³⁺, which led to improved catalytic activity. These properties result in enhanced polysulfide capture and stable rate performance in the Fe–NSC-based LSBs.

Keywords Lithium–sulfur battery · Single-atom structure · Lithium polysulfide · Catalytic host · Fe–N–S-doped carbon composite

Introduction

Lithium–sulfur batteries (LSBs) have emerged as prominent candidates for advanced battery systems [1, 2]. LSBs offer significant advantages, including a higher specific energy density (2600 Wh kg⁻¹) and a remarkable theoretical capacity (1675 mAh g⁻¹), surpassing Li-ion batteries. Moreover, sulfur, being abundant and cost-effective, presents minimal

environmental, health, and safety concerns [3]. Despite these promising attributes, LSBs face substantial challenges. The inherent non-conductive properties of sulfur species hinder vital electron transfer; while, soluble lithium polysulfide (LIPS) (Li₂S_x, 4 ≤ x ≤ 8) migrates between the anode and cathode, resulting in the reduction of active materials and depletion of the lithium anode [4, 5]. Furthermore, sluggish redox kinetics initiate LiPS accumulation at the cathode, intensifying the shuttle effect. Therefore, the practical LSBs suffer from rapid capacity degradation, short lifespan, and low Coulombic efficiency [6].

To address these intricate challenges, the development of carbon-based materials with high porosity and surface area have been proposed [7–12]. The integration of carbon materials with sulfur has been explored to facilitate electron transfer and to confine soluble LiPSs physically [13, 14]. However, the weak physical interaction between polar LiPSs and nonpolar carbon hosts hinders effective LiPS immobilization, resulting in poor cycle stability. To circumvent this limitation, heteroatom doping has been explored to introduce partial polarity into carbon-based materials, enabling strong chemical adsorption of LiPSs [15]. Although

✉ Inho Nam
inhonam@cau.ac.kr

✉ Won Suk Jung
jungw@hknu.ac.kr

¹ Department of Intelligent Energy and Industry, Department of Advanced Materials Engineering, School of Chemical Engineering and Materials Science, Chung-Ang University, Seoul 06974, Republic of Korea

² NASA Ames Research Center, Universities Space Research Association, Moffett Field, CA 94035, USA

³ School of Food Biotechnology and Chemical Engineering, Research Center of Chemical Technology, Hankyong National University, Anseong 17579, Republic of Korea

various heteroatom-doped carbon-based sulfur hosts show enhanced electrochemical performance, the optimization of these materials remains a work in progress. The predominant challenge in optimizing these complex materials is the accurate control of the heteroatom dispersion. This necessitates precise control of material parameters during synthesis and a more reliable comprehension of the relationship between electrochemical mechanisms and structural performance [16].

Herein, we report a simple synthesis of a single iron–nitrogen–sulfur-doped carbon (Fe–NSC) composite as an LSB host. Fe–N–C (Fe–NC) composites have been extensively utilized in areas such as CO₂ reduction [17], hydrogen evolution [18], and oxygen reduction reaction (ORR) [19] owing to its high activity, durability, and efficient utilization of metal atoms [20–22]. By incorporating sulfur into the Fe–NC composite, we demonstrated that this novel Fe–NSC Lithium–sulfur host offers several advantages for LSBs. First, Fe-based catalysts can potentially exhibit chemical adsorption and/or catalytic effects on lithium polysulfides (LiPS), along with a low discharge potential, making them promising hosts. Moreover, Fe acts as an effective catalyst to encourage the graphitization of carbon sources at high temperatures [23, 24]. Graphitic carbon exhibits notably higher electrical conductivity compared to amorphous carbon. The presence of partially graphitized carbon nanostructures facilitates electron transfer from insulating sulfur, enhancing overall conductivity [25]. Second, nitrogen-rich NC offers abundant and uniform pyridinic nitrogen coordination, precisely confining the arrangement of Fe–N–C species. Third, sulfur, which is a highly effective non-metallic dopant with low electronegativity, can be easily incorporated into carbon materials, facilitating effective control of the electronic properties of the Fe–N_x moieties [26]. In addition, the incorporation of sulfur improves the dispersion of Fe and increases the proportion of highly active Fe³⁺ species. Therefore, the developed Fe–NSC host effectively captured polysulfides and demonstrated stable rate characteristics when used as a host material in LSBs.

Experimental

Synthesis of Fe–NSC and Fe–NC

Activated carbon (AC, Ketjen black) was subjected to pretreatment using 13 M nitric acid at 85 °C for 8 h, followed by filtration and washing with de-ionized water (DI water) until reaching a pH of 5. The material was then dried at 80 °C. A solution containing 7.56 mmol of 1,2-ethanedithiol (EDT, 98%) was added to a 50 mL solution of 0.15 M Ethane-1,2-diamine (EDA, 99%). After stirring this mixture for 30 min, it was combined with another 50 mL solution

of 0.15 M EDA and stirred for an additional 30 min. Subsequently, this mixture was blended with a 50 mL solution containing 17.6 mM Fe(NO₃)₃•9H₂O (98%) to form a Fe–N and –S bonding [27]. Fe–NC was synthesized by mixing 25 mL of a 0.3 M N precursor solution with 50 mL of a 17.6 mM Fe precursor solution, creating the Fe–N bond. Then, this mixture was added to AC that had been pre-oxidized in isopropyl alcohol (IPA), and it was refluxed for three hours at 80 °C. Afterward, it was dried, and the resulting powder was heated for one hour at 800 °C in a nitrogen (N₂) atmosphere. The structural details and characteristics of both Fe–NC and Fe–NSC have been previously described in our research paper [27]. The Raman spectra of Fe–NSC and Fe–NC showed that Fe–NSC exhibits similar I_D/I_G values to those of AC, indicating that Fe atoms are atomically dispersed within the defects of the carbon structure. EXAFS analysis validated the Fe–N, Fe–S, and Fe–C coordination, respectively. There are no peaks for the Fe–Fe bond, which indicates the absence of Fe clusters.

Preparation of Fe–NSC/S Electrode

To prepare the Fe–NSC/S composite, a melt-diffusion method was employed. The Fe–NSC and sulfur were uniformly mixed with a 1:4 mass ratio in a mortar and then heated in a muffle furnace at 155 °C for 12 h. After cooling to room temperature, the Fe–NSC/S composite was obtained.

Adsorption Test for Li₂S₆ Solution

A Li₂S₆ solution (5 mM) was prepared by reacting Li₂S (4.6 mg) and S (9.6 mg) in 20 mL of a mixture of 1,3-dioxalane (DOL) and 1,2-dimethoxyethane (DME) in a 1:1 volume ratio. Then, it was heated to 90 °C with continuous stirring inside a glovebox for 24 h. During the reaction, the solution changed in color from white to yellow. The fabricated Li₂S₆ solution was then employed in the adsorption test, demonstrating the ability of the Fe–NSC host in trapping polysulfides.

Physical Characterization

The Fe–NSC structure was investigated using high-angle annular dark-field image-scanning transmission electron microscopy–energy dispersive X-ray spectroscopy (HAADF-STEM-EDS) and high-resolution transmission electron microscopy (HR-TEM) with the FEI TalosTM F200X. Furthermore, field-emission scanning electron microscopy (FE-SEM, SIGMA 300, Carl Zeiss) was used to analyze the morphologies and material compositions. X-ray diffraction (XRD, Rigaku Smartlab) was performed to confirm the Fe–NSC structure. X-ray photoelectron

spectroscopy (XPS, PHI 5000 VersaProbe) was performed to determine the chemical compositions of Fe–NSC and Fe–NC. Thermogravimetric analysis (TGA) was conducted from 25 to 400 °C in aluminum crucibles in N₂ flow.

Electrochemical Analysis

The AC/S composite and Fe–NSC/S composite, Super P, and poly(vinylidene fluoride) (PVdF; weight ratio, 8:1:1) were mixed to fabricate the working electrodes. The prepared slurry was applied to an Al foil current collector. Subsequently, it was dried at 60 °C for 12 h under vacuum conditions. Each electrode was loaded with sulfur with an approximate weight of 1 mg cm⁻². The 2032 coin cells were assembled in an Ar-filled glovebox, using Li foil as a counter electrode and Celgard 2400 as a separator. The electrolyte was 1.0 M lithium bis(trifluoromethyl sulfonyl) imide (LiTFSi) in 1,3-dioxolane (DOL)/1,2-dimethoxyethane (DME) in a 1:1 volume ratio, with 1 wt% lithium nitrate (LiNO₃) as an additive. The electrolyte-to-sulfur (E/S) ratio was approximately 20 μL mg⁻¹. Galvanostatic

charge–discharge (GCD) measurements were conducted at 25 °C in the voltage range of 1.6–2.8 V using a cycler (WonATech).

Results and Discussion

Fe–N–S–C (Fe–NSC) composites were synthesized following the process illustrated in Fig. 1a. Initially, pre-oxidized AC (Ketjen black) was prepared. Subsequently, Fe–NSC composites were prepared via chelation with Fe, N, and S and a subsequent annealing. The Fe–NC composite has a bush-like morphology, as shown in Fe-SEM images (Fig. 1b). Aggregated particles of Fe species are observed in the HR-TEM images of the Fe–NC (Fig. 1c). However, the simultaneous addition of N and S precursors results in a homogeneously dispersed microstructure and morphology of the synthesized Fe–NSC. HAADF-STEM with aberration correction was utilized to observe Fe single atoms. Numerous individual bright dots representing Fe atoms are distinctly observed and highlighted by white circles (Fig. 1e). Elemental mapping of Fe–NSC confirmed the

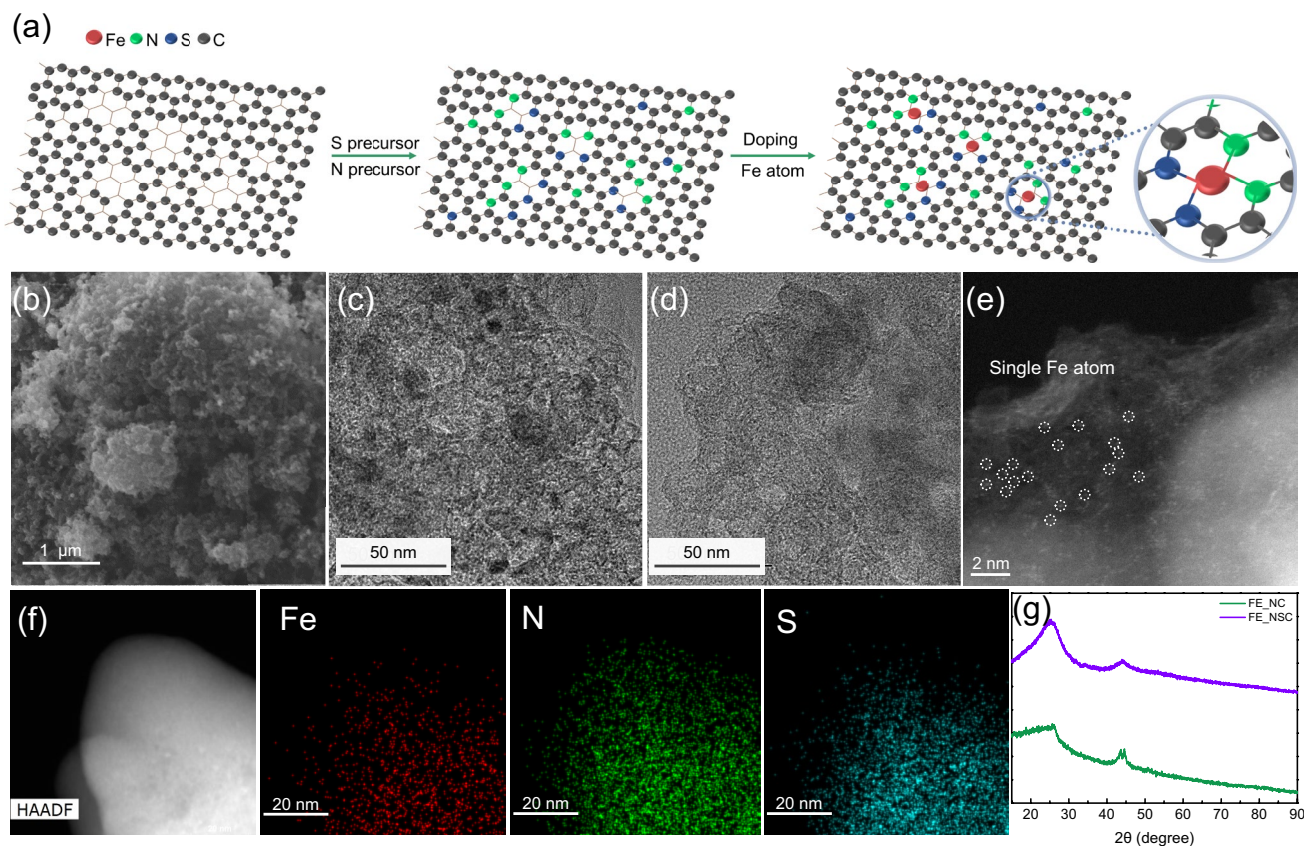


Fig. 1 a Schematic of Fe–NSC synthesis, b FE-SEM images of Fe–NC; HR-TEM image of c Fe–NC, and d Fe–NSC, e STEM image of single Fe atom on NSC, f HAADF-STEM image (scale bar: 20 nm)

and corresponding element mapping (Fe, N, and S), g XRD pattern of Fe–NC and Fe–NSC

uniform distribution of Fe, N, and S (Fig. 1f). Furthermore, the XRD patterns show the existence of a pure carbon structure without metal particles within the Fe–NSC structure (Fig. 1g). Fe–NSC displayed distinctive peaks at about 25.3° and 43.9° , which corresponded to the amorphous carbon (002) and graphitic carbon (100) planes, respectively. The absence of additional diffraction peaks associated with Fe-based compound indicates a high dispersion of the Fe components, which is consistent with HR-TEM data.

To gain insights into the interaction between Fe single atoms and the N–S–C structure, we conducted X-ray photoelectron spectroscopy (XPS). The obtained XPS spectra distinctly display peaks corresponding to N_{1s} , Fe_{2p} , C_{1s} , O_{1s} , and S_{2p} within the Fe–NSC composite, with a nitrogen atomic ratio of approximately 3.11 at% (Table 1). Because of the limited detection depth of XPS (usually ranging from 1 to 10 nm) and low Fe content, the Fe peak exhibited a low

intensity. This suggests that Fe single atoms are embedded in the NSC, consistent with the TEM observation. The N_{1s} XPS profiles of both Fe–NSC and Fe–NC is presented in Fig. 2a, d. These indicate that the nitrogen atoms in the Fe–NSC composite adopt diverse forms, including pyridinic (398.4 eV), $Fe-N_x$ (399.8 eV), pyrrolic (400.7 eV), graphitic (401.5 eV), and oxidized nitrogen groups (403.6 eV) [28]. The N_{1s} XPS results indicate that 38% of the nitrogen in the Fe–NSC sample is pyridinic and 7% is also coordinated with Fe atoms ($Fe-N_x$). In contrast, 31% of the nitrogen in the Fe–NC sample is pyridinic and no evident $Fe-N_x$ coordination is detected. The Fe single atoms on the NSC host predominantly form bonds with pyridinic N. Consequently, the dispersion and concentration of N in the NSC host play critical roles in immobilizing the uniformly dispersed Fe single atoms through chemical coordination. In the high-resolution Fe 2p XPS spectrum of both Fe–NSC and Fe–NC, 6 peaks were fitted, representing the oxidation states of iron (Fig. 2b, e). Fe–NC could be deconvoluted into three peaks correspond to Fe^0 , Fe^{2+} , and Fe^{3+} . Fe^0 peaks are located at 720.5 eV ($2p_{3/2}$) and 707.3 eV ($2p_{1/2}$). Fe^{2+} peaks are 723.6 eV ($2p_{1/2}$) and 710.6 eV ($2p_{3/2}$). The other peaks at 728.6 eV ($2p_{1/2}$) and 715.9 eV ($2p_{3/2}$) were attributed to Fe^{3+} [29, 30]. In the Fe–NSC composite, Fe 2p spectrum was deconvoluted into six peaks at 710.6 ($2p_{3/2}$), 713.4 ($2p_{3/2}$), 717.6 ($2p_{3/2}$),

Table 1 XPS analysis results of Fe–NC and Fe–NSC

	C 1s (at.%)	N 1s (at.%)	S 2p (at.%)	O 1s (at.%)	Fe 2p (at.%)
Fe–NC	97.1	1.26	–	1.53	0.11
Fe–NSC	88.9	3.11	5.29	2.61	0.08

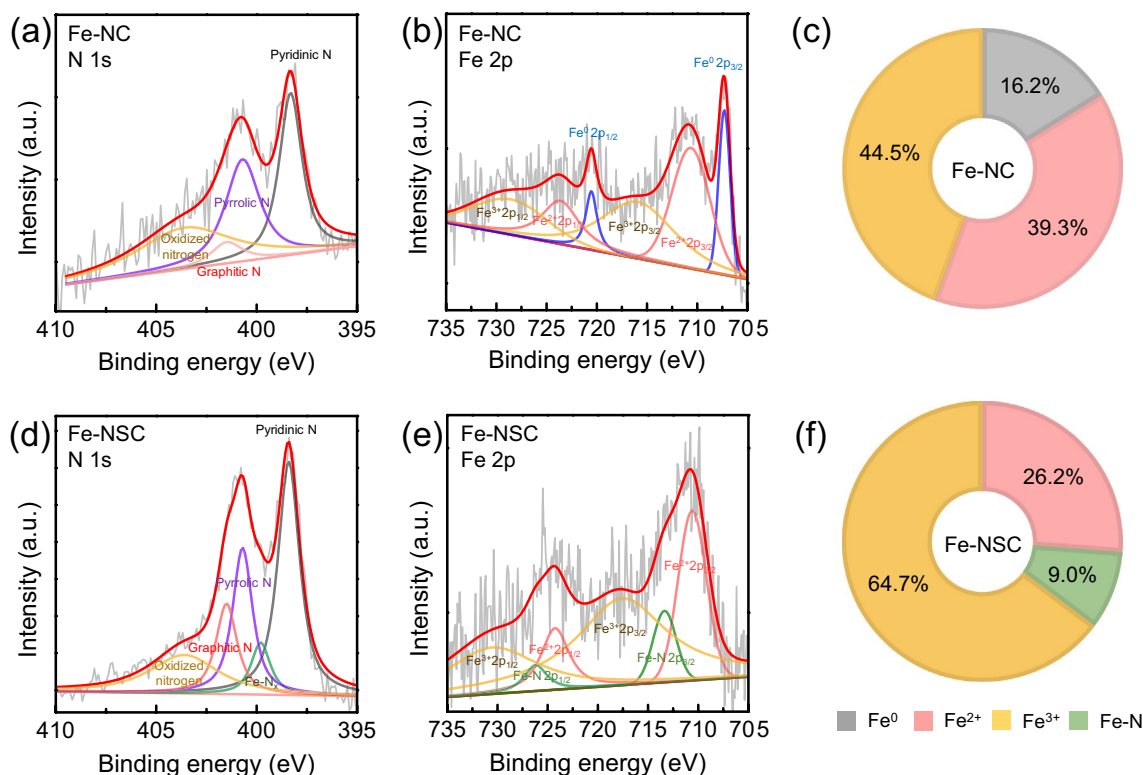


Fig. 2 High-resolution XPS spectra of Fe–NC in **a** N_{1s} **b** and Fe 2p, **c** contents of Fe bonding configurations of Fe–NC; high-resolution XPS spectra of Fe–NSC in **d** N_{1s} and, **e** Fe 2p, **f** contents of Fe bonding configurations of Fe–NSC

724.2 ($2p_{1/2}$), 726.2 ($2p_{1/2}$), and 730.5 eV ($2p_{1/2}$), which are Fe^{2+} , Fe-N_x , and Fe^{3+} , respectively. We confirmed that Fe^{3+} ratio is 64.7%, which is higher than that of Fe^{2+} (Fig. 2c, f). The incorporation of S increased the ratio of Fe^{3+} and promoted a uniform dispersion of Fe. Fe^{3+} contributes significantly to the polysulfide reduction reaction because of its low spin state, which hinders electron acceptance and provides more active sites than Fe^{2+} [31].

Pore analysis was performed on the Fe–NSC composites to gain insights into the possible sulfur loading amount. The porous structures in both Fe–NSC and Fe–NC were demonstrated by the N_2 adsorption–desorption isotherms. The specific pore volume and surface areas of Fe–NSC were $0.503 \text{ cm}^3 \text{ g}^{-1}$ and $340.13 \text{ m}^2 \text{ g}^{-1}$, respectively. Notably, Fe–NSC exhibited a larger specific surface area than Fe–NC ($301.84 \text{ m}^2 \text{ g}^{-1}$), which implies that sulfur doping might induce structure distortion and additional defects. To optimize the sulfur loading ratio, the Fe–NSC composites were loaded with elemental S using the melt-impregnation method. After sulfur was incorporated, pore volume and the specific surface area of Fe–NSC decreased sharply in $0.268 \text{ cm}^3 \text{ g}^{-1}$ and $15.679 \text{ m}^2 \text{ g}^{-1}$, respectively. This observation was consistent with the anticipated effect of accommodating sulfur within the substantial void space and high specific surface area.

To assess the catalytic effectiveness of Fe–NSC, we prepared an AC sample without metal atom doping as a control. Sulfur was loaded onto both Fe–NSC (Fe–NSC/S) and AC (AC/S). The XRD patterns of sulfur, AC/S, and Fe–NSC/S composites are depicted in Fig. 3a. AC/S shows distinct and strong sulfur peaks, implying the predominant presence of sulfur on the surface of AC/S. Comparatively weak sulfur peaks are evident in the Fe–NSC/S composite compared to AC/S. These XRD results indicate effective sulfur diffusion into the pores of Fe–NSC. The final sulfur content in Fe–NSC/S and AC/S was quantified through TGA analysis, as depicted in Fig. 3b. Pure sulfur shows a single-slope curve during sublimation, at approximately 150–230 °C. The steep

slope indicates easier volatilization of S from the host. At temperatures below 230 °C, the TGA curves of AC/S closely align with that of pure sulfur, indicating negligible adhesion between the hosts and sulfur. On the other hand, the TGA curves of Fe–NSC/S appear as a significantly gentler slope up to 300 °C. This indicates the strong confinement of sulfur in Fe–NSC. The enhanced adhesion of sulfur in Fe–NSC plays a critical role in stable ion transport within the sulfur cathode, thereby contributing to improved sulfur utilization. To prove the utility of Fe–NSC as a sulfur host, the rate capabilities were compared with AC, which is commonly used as a sulfur host, by increasing the current rate from 0.1 to 4 C (Fig. 3c). The specific capacities of Fe–NSC/S measured 560.3, 406.5, 319.7, 267.2, 223.0, and 161.4 mAh g^{-1} at 0.1, 0.2, 0.5, 1, 2, and 4 C, respectively. These are higher than those of the AC/S cathode, which measured 278.6, 229.8, 161.3, 117.8, 81.5, and 55.9 mAh g^{-1} , respectively. The capacity gap between Fe–NSC/S and AC/S is as much as $\approx 168.9 \text{ mAh g}^{-1}$ at the same current rates. These data indicate that the Fe–NSC host has an electrocatalytic effect to enhance the rate capabilities. Galvanostatic charge–discharge (GCD) at 0.1 C for activation cycles was used to evaluate the electrochemical performance of Fe–NSC as a sulfur host in LSB cathodes. Depending on the amount of sulfur in the Fe–NSC composite, we denoted it as Fe–NSC α , where α is the percentage amount of the sulfur. The cycle performance between 1.6 and 2.8 V at 0.1 C of Fe–NSC54, Fe–NSC60, and Fe–NSC75 are displayed in Fig. 4. A small shoulder located at about 1.6 V in the first cycle is caused by the irreversible decomposition of the LiNO_3 additive on the cathode.

To evaluate the rate performance of Fe–NSC cathodes depending on the weight percent, we conducted battery tests at various current rates (C-rates) as shown in Fig. 5. As the C-rate was increased, the voltage gap between charge and discharge plateaus was enlarged. Among the different sulfur content of Fe–NSC samples, Fe–NSC60 exhibits the highest capacity. As the C-rates increased, reversible capacities

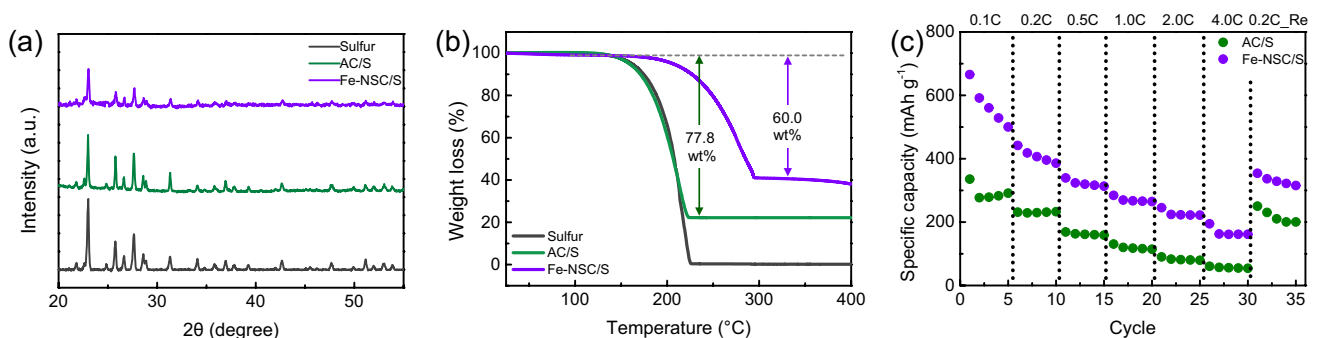


Fig. 3 **a** XRD patterns of pristine sulfur, AC/S, and Fe–NSC/S composite. **b** TGA curves of sulfur, AC/S, and Fe–NSC/S composite at a temperature range of 25–400 °C. **c** Rate capabilities of AC/S and Fe–NSC/S electrodes

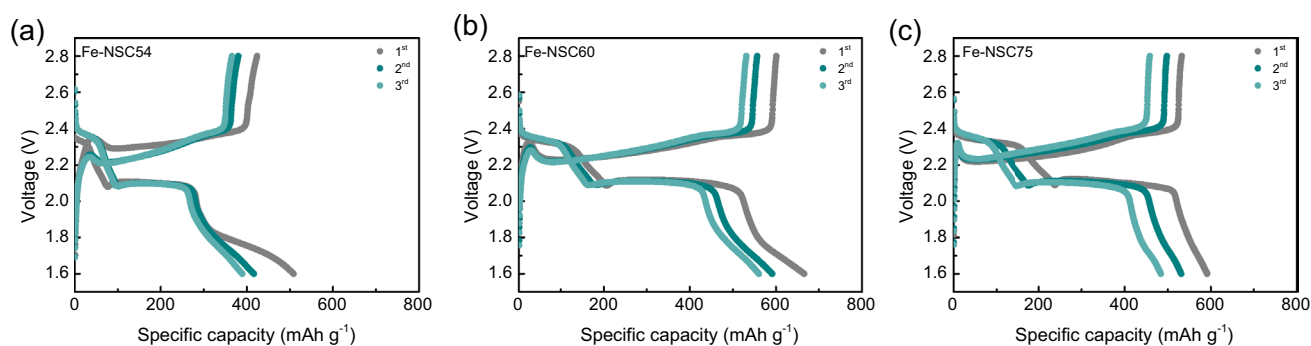
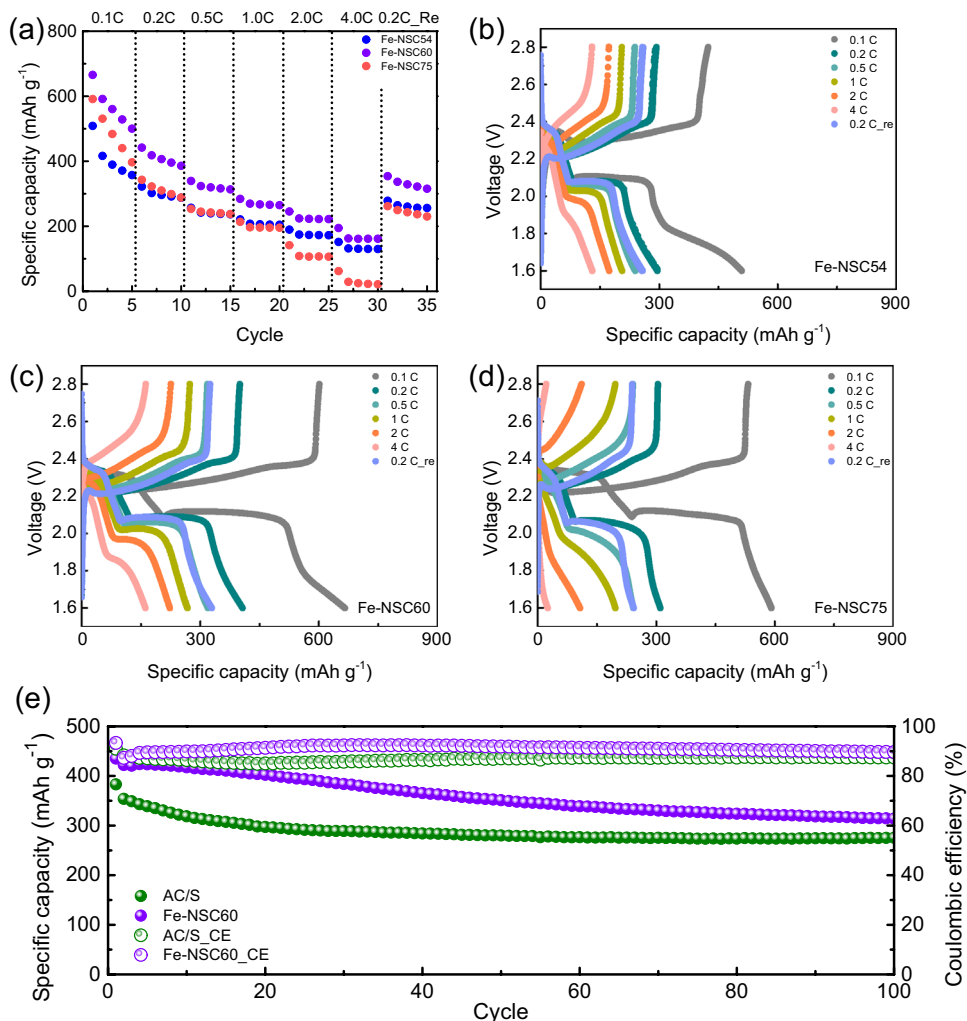


Fig. 4 Comparative performance of LSBs in the first and third formation cycles for **a** Fe-NSC54, **b** Fe-NSC60, and **c** Fe-NSC75

Fig. 5 **a** Rate performance based on Fe-NSC. GCD curves of batteries based on Fe-NSC: S ratio at 0.1–4 C. **b** Fe-NSC54, **c** Fe-NSC60, **d** Fe-NSC75, **e** long cycle performance of AC/S and Fe-NSC60 at 0.2 C



were measured as 560.3, 406.5, 319.7, 267.2, 223.0, and 161.4 mAh g^{-1} at C-rates of 0.1, 0.2, 0.5, 1, 2, and 4 C, respectively. When the sulfur content in the Fe-NSC host was increased to 75%, the discharge plateaus almost vanished at above 2 C, indicating that the sulfur was coated on the outside. Based on the results above, Fe-NSC60 provides

promising cell performance with a significant role of Fe in enhancing polysulfide reduction capability. To compare the effect with and without the introduction of single-atom Fe catalyst, we tested the long cycle performance of Fe-NSC60 and AC/S cathode at 0.2 C. One activation cycle was performed at 0.1 C. After 100 cycles, the Fe-NSC60 cathode

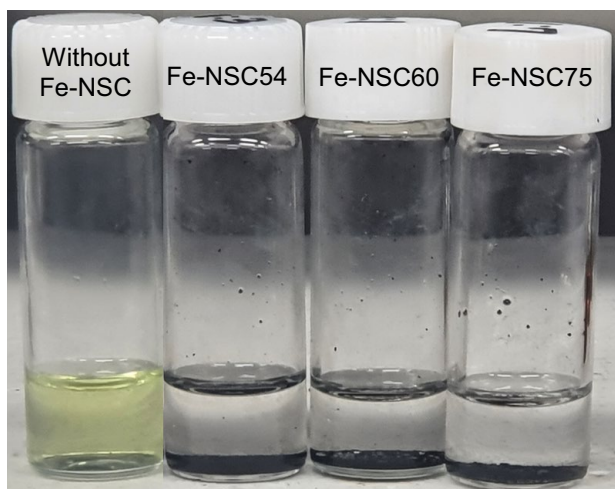


Fig. 6 Optical photograph of Li_2S_6 solution and Li_2S_6 solution with Fe–NSC composite

maintained a capacity of about 314.1 mAh g^{-1} , which is higher than that of AC/S (275.4 mAh g^{-1}) (Fig. 5e). It suggests that a single-atom Fe catalyst could improve cycle performance.

Further, we examined the adsorption capabilities of Fe–NSC with varying sulfur content, as depicted in Fig. 6. Initially, a composite of 5 mg Fe–NSC was mixed with 5 mL of Li_2S_6 solution (10 mmol/L) in a solvent mixture of DOL/DME (1:1 v/v) [32]. The polysulfide adsorption capacity plays a pivotal role in selecting a suitable material for chemically confining the soluble lithium polysulfides generated within the cathode. To explore the adsorption capability of Fe–NSCs for polysulfides, Li_2S_6 was chosen as a model due to its prominent properties among soluble LiPSs (Li_2S_x , $4 \leq x \leq 8$) as the cell cycling progresses. Li_2S_6 has the highest stability in the electrolyte and is more likely to migrate toward the anode than other soluble LiPSs because of its reduction to Li_2S during the discharge process. To identify the most effective Fe–NSC sample with optimal polysulfide adsorption capabilities, the color changes of Li_2S_6 solutions were monitored using a digital camera after 24 h [33]. Interestingly, the Fe catalyst induced the complete fading of Li_2S_6 solution color, irrespective of the loaded sulfur content, signifying the proficient polysulfide adsorption ability of the material.

Conclusions

This study demonstrates a novel approach employing a single Fe–NSC composite as a host material for Fe–NC nanocatalysts, commonly applied in CO_2 reduction, hydrogen evolution, and oxygen reduction. The introduction of sulfur into the Fe–NC structure yielded three significant

enhancements in performance: improved dispersion of the Fe catalyst, a high surface area, and an increased proportion of Fe^{3+} , leading to improved catalytic activity. The successful adsorption of polysulfides was also demonstrated through a polysulfide adhesion test. Notably, Fe–NSC60 exhibited an optimal sulfur loading ratio, showing more stable rate capabilities than other Fe–NSC samples.

Acknowledgements This work is supported by the National Research Foundation (NRF) grant funded by the Korea government (MSIT) (No. 2020R1C1C1004206), the Korea Institute of Energy Technology Evaluation and Planning (KETEP) funded by the Korea government (No. 2021400000280), and the Competency Development Program for Industry Specialists of the Korean government operated by KIAT (No. P0012453).

References

1. K. Zou, T. Zhou, Y. Chen, X. Xiong, W. Jing, X. Dai, M. Shi, N. Li, J. Sun, S. Zhang, C. Zhang, Y. Liu, Z. Guo, *Adv. Energy Mater.* **12**, 2103981 (2022)
2. L. Fan, M. Li, X. Li, W. Xiao, Z. Chen, J. Lu, *Joule* **3**, 361 (2019)
3. Y. Chen, T. Wang, H. Tian, D. Su, Q. Zhang, G. Wang, *Adv. Mater.* **33**, 2003666 (2021)
4. S. Li, W. Zhang, J. Zheng, M. Lv, H. Song, L. Du, *Adv. Energy Mater.* **11**, 2000779 (2021)
5. F. Li, Q. Liu, J. Hu, Y. Feng, P. He, J. Ma, *Nanoscale* **11**, 15418 (2019)
6. Y. Huang, L. Lin, C. Zhang, L. Liu, Y. Li, Z. Qiao, J. Lin, Q. Wei, L. Wang, Q. Xie, D.-L. Peng, *Adv. Sci.* **9**, 2106004 (2022)
7. C. Sun, Y. Liu, J. Sheng, Q. Huang, W. Lv, G. Zhou, H.-M. Cheng, *Mater. Horiz.* **7**, 2487 (2020)
8. Q. Zhao, Q. Zhu, Y. Liu, B. Xu, *Adv. Funct. Mater.* **31**, 2100457 (2021)
9. Z. Gu, C. Cheng, T. Yan, G. Liu, J. Jiang, J. Mao, K. Dai, J. Li, J. Wu, L. Zhang, *Nano Energy* **86**, 106111 (2021)
10. R. Wang, R. Wu, X. Yan, D. Liu, P. Guo, W. Li, H. Pan, *Adv. Funct. Mater.* **32**, 2200424 (2022)
11. R. Saroha, J.-H. Ahn, J.S. Cho, *Korean J. Chem. Eng.* **38**, 461 (2021)
12. S.-H. Yeon, W. Ahn, K.-H. Shin, C.-S. Jin, K.-N. Jung, J.-D. Jeon, S. Lim, Y. Kim, *Korean J. Chem. Eng.* **32**, 867 (2015)
13. R. Yan, M. Oschatz, F. Wu, *Carbon* **161**, 162 (2020)
14. W.-G. Lim, C. Jo, J. Lee, D.S. Hwang, *Korean J. Chem. Eng.* **35**, 579 (2018)
15. K. Liu, S. Gu, H. Yuan, H. Wang, W. Tan, F. Jiang, J. Chen, K. Liao, C. Yan, F. Yang, Z. Lu, Z. Xu, *Compos. Commun.* **30**, 101079 (2022)
16. X. Zhou, R. Meng, N. Zhong, S. Yin, G. Ma, X. Liang, *Small Methods* **5**, 2100571 (2021)
17. J. Zhao, J. Deng, J. Han, S. Imhanria, K. Chen, W. Wang, *Chem. Eng. J.* **389**, 124323 (2020)
18. M. Hu, Z. Cai, S. Yang, Z. Wang, F. Shen, X. Liang, G. Sun, H. Ren, Y. Cao, B. Hu, S. Liu, H. Tan, K. Zhou, *Adv. Funct. Mater.* **33**, 2212097 (2023)
19. L. Li, Y. Wen, G. Han, Y. Liu, Y. Song, W. Zhang, J. Sun, L. Du, F. Kong, Y. Ma, Y. Gao, J. Wang, C. Du, G. Yin, *Chem. Eng. J.* **437**, 135320 (2022)
20. H.-E. Kim, S. Jang, H. Lim, W. Chung, I. Nam, J.H. Bang, *Appl. Surf. Sci.* **624**, 157161 (2023)

21. Y. Wang, A. Cho, G. Jia, X. Cui, J. Shin, I. Nam, K.-J. Noh, B.J. Park, R. Huang, J.W. Han, *Angew. Chem. Int. Ed.* **62**, e202300119 (2023)
22. J. Hwang, *Korean J. Chem. Eng.* **38**, 1104 (2021)
23. X. Cui, L. Gao, S. Lei, S. Liang, J. Zhang, C.D. Sewell, W. Xue, Q. Liu, Z. Lin, Y. Yang, *Adv. Funct. Mater.* **31**, 2009197 (2021)
24. L. Yu, Y. Li, Y. Ruan, *Angew. Chem. Int. Ed.* **60**, 25296 (2021)
25. S. He, J. Yang, S. Liu, X. Wang, X. Che, M. Wang, J. Qiu, *Chem. Eng. J.* **454**, 140202 (2023)
26. L. Ren, J. Liu, Y. Zhao, Y. Wang, X. Lu, M. Zhou, G. Zhang, W. Liu, H. Xu, X. Sun, *Adv. Funct. Mater.* **33**, 2210509 (2023)
27. H.S. Yoon, B.Y. Lim, H.Y. Park, S.-K. Kim, W.S. Jung, *J. Electroanal. Chem.* **948**, 117813 (2023)
28. M. Ayiania, M. Smith, A.J.R. Hensley, L. Scudiero, J.-S. McEwen, M. Garcia-Perez, *Carbon* **162**, 528 (2020)
29. C. Ling, S. Wu, T. Dong, H. Dong, Z. Wang, Y. Pan, J. Han, *J. Hazard. Mater.* **423**, 127082 (2022)
30. Z. Liu, F. He, L. Zhou, Z. Li, L. Zhong, J. Ding, *J. Chem. Technol. Biotechnol.* **98**, 1731 (2023)
31. Z. Chen, H. Niu, J. Ding, H. Liu, P.-H. Chen, Y.-H. Lu, Y.-R. Lu, W. Zuo, L. Han, Y. Guo, S.-F. Hung, Y. Zhai, *Angew. Chem. Int. Ed.* **60**, 25404 (2021)
32. D.-R. Deng, T.-H. An, Y.-J. Li, Q.-H. Wu, M.-S. Zheng, Q.-F. Dong, *J. Mater. Chem. A* **4**, 16184 (2016)
33. J.H. Ahn, G.K. Veerasubramani, S.-M. Lee, T.-S. You, D.-W. Kim, *J. Electrochem. Soc.* **166**, A5201 (2018)

Publisher's Note Springer Nature remains neutral with regard to jurisdictional claims in published maps and institutional affiliations.

Springer Nature or its licensor (e.g. a society or other partner) holds exclusive rights to this article under a publishing agreement with the author(s) or other rightsholder(s); author self-archiving of the accepted manuscript version of this article is solely governed by the terms of such publishing agreement and applicable law.